

A Transition from Fine to Coarse Lamellar Eutectics in the Undercooled Ni-29.8 At. Pct Si Eutectic Alloy: Experiments and Modeling



FAN ZHANG, HAIFENG WANG, M. KOLBE, JIANBAO ZHANG, QING ZHOU,
and D.M. HERLACH

In contrast to the classical eutectic growth models, according to which the eutectic spacing decreases invariably with undercooling, an anomalous transition from fine to coarse lamellar eutectics was found in the undercooled Ni-29.8 at. pct Si eutectic alloy. In this study, the growth kinetics, recalescence processes, and grain orientations were analyzed. A sharp increase of the growth velocity at an undercooling of about 100 K was found. The recalescence front transitioned in sequence from a diffuse one with tips, to a diffuse one without tips and then to a sharp one. The microstructures changed from a mixture of directional rod-shaped γ -Ni₃₁Si₁₂ grains and fine lamellar eutectics to solely coarse lamellar eutectics. Coarse lamellar eutectics were found to be formed by rapid solidification of primary directional rod-shaped Ni₃₁Si₁₂ intermetallic compound and subsequent epitaxial growth of secondary Ni₂Si intermetallic compound, being consistent with the predictions of eutectic-dendritic and dendritic growth models. Coarse anomalous eutectics at low undercooling were formed by fragmentation of fine lamellar eutectics and their subsequent coarsening. At high undercooling, they were formed by decoupled-eutectic growth.

<https://doi.org/10.1007/s11661-019-05221-0>

© The Minerals, Metals & Materials Society and ASM International 2019

I. INTRODUCTION

EUTECTIC alloys are not only important conventional engineering materials (*e.g.*, the graphite cast iron and the Al-Si cast aluminium alloys^[1]) but also potential new materials (*e.g.*, the eutectic high entropy alloys^[2,3]). Under rapid solidification conditions, eutectic alloys exhibit some non-equilibrium microstructures,^[4] the study of which is not only of scientific significance to understand microstructure formation but also of practical importance to improve material properties.

From the classical eutectic growth model of Jackson and Hunt (JH),^[5] $V^2\lambda = K$ holds (V is the growth velocity, λ is the eutectic spacing,* and K is a constant

*For lamellar eutectics, λ is the lamellar spacing, while for rod eutectics, λ is the sum of the radiuses of constituent phases.

depending on the alloy properties). Accordingly, the eutectic spacing decreases with increasing growth velocity. After an extension of the JH model^[5] to rapid solidification, Trivedi *et al.*^[6–8] found that K is dependent on the growth velocity and eutectic spacing. Consequently, there is a maximum growth velocity for eutectic growth. If growth is directional, the growth velocity increases but the eutectic spacing decreases with undercooling. If growth takes place in an undercooled melt, the growth velocity first increases and then decreases with undercooling while the eutectic spacing decreases invariably.^[7] At the maximum growth velocity, the eutectic spacing is usually on the nanoscale, indicating that rapid solidification of eutectic alloys is a useful method to prepare *in-situ* nanoscale composites.^[8] For example, Wang *et al.*^[7] carried out a systematic experimental study on the Al-Sm eutectic alloy over a wide range of undercooling. Using the melt spinning technique, the eutectic spacing of the Al-38 wt pct Sm

FAN ZHANG, HAIFENG WANG, JIANBAO ZHANG, and QING ZHOU are with the State Key Laboratory of Solidification Processing, Center of Advanced Lubrication and Seal Materials, Northwestern Polytechnical University, Xi'an, Shaanxi 710072, P.R. China. Contact e-mail: haifengw81@nwpu.edu.cn M. KOLBE is with the Institut für Materialphysik im Weltraum, Deutsches Zentrum für Luft-und Raumfahrt (DLR), 51170 Cologne, Germany. D.M. HERLACH is with the Ruhr-Universität Bochum, Fakultät für Physik und Astronomie, 44780 Bochum, Germany. Contact e-mail: Dieter.Herlach@dlr.de

Manuscript submitted December 24, 2018.

Article published online April 15, 2019

hypereutectic alloy can be as low as 17 nm. Combining the melt fluxing technique with Cu-mold casting, Huang *et al.*^[9] reduced the lamellar spacing of Fe-B-Si and Fe-B-Cu ternary alloys to less than 50 nm, thus improving considerably the soft magnetic properties.

In undercooled melts of eutectic alloys, eutectic growth does not hold always. For eutectic alloys with a symmetric coupled zone, eutectic growth is always the case. For eutectic alloys with a skewed coupled zone, however, a transition from eutectic growth to single-phase dendritic growth occurs. Furthermore, re-melting as a result of the chemical superheating effect^[10–12] and/or fragmentation as a result of Rayleigh instability^[13–16] might make the initial microstructure inevitably transit into anomalous eutectics^{**}. Therefore,

^{**}The formation mechanism of anomalous eutectics was widely studied. But it is still in debate even for the same eutectic alloys.^[12,16–25]

it is difficult to retain the initial non-equilibrium microstructures (*e.g.*, the refined lamellar eutectics) to room temperature. Nevertheless, lamellar eutectics were found in highly undercooled Ni-19.6 at. pct P^[12] and Ni-29.8 at. pct Si^[26] eutectic alloys[†]. For the former, the

[†]For both the Ni-19.6 at. pct P and Ni-29.8 at. pct Si eutectic alloys, the constituent eutectic phases are two stoichiometric intermetallic compounds. In this case, solute supersaturation is completely absent to avoid the chemical superheating effect.

lamellar spacing decreases considerably with undercooling.^[12] For the latter, a transition from fine to coarse lamellar eutectics happens.^[27] Such an increase of lamellar spacing with undercooling in the undercooled Ni-29.8 at. pct Si eutectic alloy is inconsistent with the eutectic growth models.^[5–8]

In current work, rapid solidification of undercooled Ni-29.8 at. pct Si eutectic alloy was re-examined. The samples were processed by electromagnetic levitation (EML). Compared with the melt fluxing technique used in previous work,^[26,27] the sample was rotating during our levitation experiments. Consequently, the nucleation site could be easily observed and the whole solidification process could be recorded. Furthermore, due to the forced gas cooling, the achieved cooling rate during solidification is much large. The recalescence process was recorded by a high-speed camera to measure the growth velocity. The microstructures were analyzed by electron back-scattering diffraction (EBSD) to obtain the grain orientations. Coarse lamellar eutectics at high undercooling were found to be formed by rapid solidification of a primary directional rod-shaped Ni₃₁Si₁₂ intermetallic compound and subsequent epitaxial growth of a secondary Ni₂Si intermetallic compound. This formation mechanism is consistent with the predictions of the eutectic-dendritic growth model^[28–31] and dendritic growth model.^[32,33] Origins and formation mechanisms of coarse anomalous eutectics were discussed.

II. EXPERIMENTAL

Samples of the Ni-29.8 at. pct Si eutectic alloy with a mass of 1 g were prepared from the high-purity elements Ni (99.999 pct) and Si (99.999 pct). The samples were alloyed in an arc melting furnace which was previously evacuated to a pressure of 10⁻⁶ mbar and subsequently filled by argon (99.9999 pct) to a pressure of 1 bar.

Containerless processing by EML was adopted for the present solidification study. With EML, heterogeneous nucleation on the container wall can be completely avoided. Hence, it is possible to achieve high undercooling. The sample was positioned within an inhomogeneous electromagnetic field generated by alternating currents through a levitation coil. The chamber was evacuated first to a pressure of 1×10⁻⁶ mbar and then back filled by helium (99.9999 pct) to a pressure of 0.3 bar. After levitating the sample and heating it to 200 K to 300 K above the eutectic melting temperature, the temperature was held for 3 to 5 minutes. Then, the power of the coil was reduced to a lower value, at which the sample can be still levitated. After that, helium was introduced from the bottom of chamber to cool down the melt. A high-speed camera (Photron Ultima APX with adjustable frame rates up to 120000 fps) was used to record the recalescence process. A two-color pyrometer with an accuracy of ± 5 K and a measurement frequency of 100 Hz was adopted to measure the thermal history. Each sample was cyclically superheated and cooled down to achieve a wide range of undercooling or a desired undercooling.

The as-solidified samples were successively mounted in epoxy resin, ground, and polished. The microstructures were examined by optical microscopy and scanning electron microscopy (SEM, LEO 1530 VP by Zeiss). After polishing the samples by the SiO₂ colloidal suspension, the grain orientations were studied by EBSD in a SEM equipped with a Channel 5 EBSD analysis system. The step size is set to be 1 μm or 0.1 μm during orientation mapping.

III. RESULTS

A. Cooling Curves

Figure 1 shows some typical cooling curves for the samples with desired undercooling ranging from a low undercooling of $\Delta T = 42$ K to the highest undercooling of $\Delta T = 228$ K achieved in current work. For all the cases, only a single recalescence event was found. This is different to previous work using the melt fluxing technique,^[27] where two recalescence events were found at intermediate undercooling. The reason might be that the higher cooling rate due to forced gas cooling in EML enabled to retain the initial solidification microstructures, whereas in Reference 27 the samples were cooled down much slower to room temperature due to thermal transport *via* the melt flux. Furthermore, oscillation of the samples upon solidification in the case of using EML may lead to fluctuation in the temperature curves, which might make the recalescence events indistinguishable.

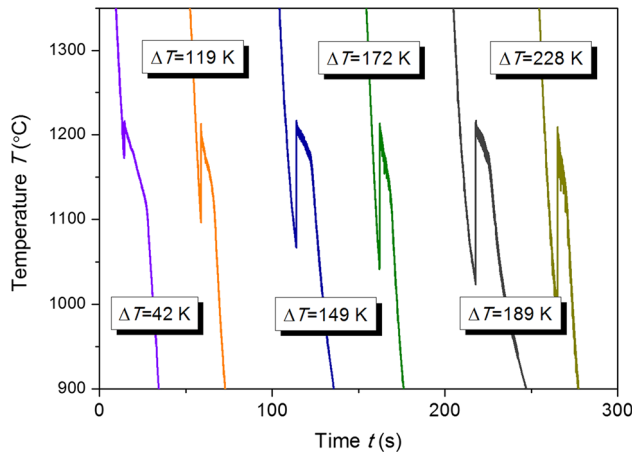


Fig. 1—Typical cooling curves for rapid solidification in the undercooled Ni-29.8 at. pct Si eutectic alloy.

However, a single recalescence event observed in current work does not mean that the microstructures are solely eutectics as shown in what follows[‡].

[‡]Generally, the recalescence events can be used to understand the solidification processes, *e.g.*, one recalescence event usually corresponds to one solidification process. This is, however, not the case if multiple nucleation events happen within the sample or epitaxial growth of the second phase on the primary phase occurs, *e.g.*, in current work.

B. Microstructures

From the Ni-Si phase diagram,^[34–36] the two consistent phases are the intermetallic δ -Ni₂Si and γ -Ni₃₁Si₁₂ phases for the Ni-29.8 at. pct Si eutectic alloy. Furthermore, there are no solid-state phase transformations after eutectic solidification. Because the composition ranges of Si in the δ -Ni₂Si (26.5 to 29.5 at. pct) and γ -Ni₃₁Si₁₂ (32.5 to 34.5 at. pct) phases are negligible small,^[34] both of them were assumed to be stoichiometric in thermodynamic descriptions^{[35,36]§}.

[§]It should be pointed out in the work of Du *et al.*,^[35,36] it is the γ -Ni₅Si₂ phase that was used.

Figure 2 shows the as-solidified microstructures for the undercooled Ni-29.8 at. pct Si eutectic alloy. At low undercooling, *e.g.*, $\Delta T = 42$ K, fine lamellar eutectics are prevailing within the whole sample (Figure 2(a)) except for minor coarse anomalous eutectics at the center (Section IV-B). At intermediate undercooling, *e.g.*, $\Delta T = 85$ K and $\Delta T = 92$ K, the fragmented primary γ -Ni₃₁Si₁₂ phase distributes randomly, around which fine lamellar eutectics can be found (cf. Figures 2(b) and (c)). The primary γ -Ni₃₁Si₁₂ phase should be formed during recalescence. Fine lamellar eutectics should be formed after recalescence. When undercooling increases further, *e.g.*, $\Delta T = 119$ K, the primary γ -Ni₃₁Si₁₂ phase becomes directional and its partial fragmentation is prevailing (cf. Figure 2(d)). At

$\Delta T = 168$ K, coarse lamellar eutectics appear near the nucleation site (cf. Figure 2(e)). The remained microstructures distant from the nucleation site are similar to those at $\Delta T = 85$ K and $\Delta T = 92$ K. When undercooling is very high, *e.g.*, $\Delta T = 228$ K, only coarse lamellar eutectics can be found (cf. Figure 2(f)). The critical undercooling for the formation of solely coarse lamellar eutectics is $\Delta T = 185$ K. One can see that with increasing undercooling, an anomalous transition from fine to coarse lamellar eutectics happens.

In the undercooled Ni-29.8 at. pct Si eutectic alloy, three kinds of microstructures can be found, *i.e.*, fine lamellar eutectics, coarse lamellar eutectics, and primary rod-shaped γ -Ni₃₁Si₁₂ grains. The lamellar spacing of fine and coarse lamellar eutectics (λ_{fine} and λ_{coarse}) as well as the width of the primary rod-shaped γ -Ni₃₁Si₁₂ grains (W_{rod}) were measured (cf. Figure 3)^{§§}. One can

^{§§}It should be pointed out that except for Figure 2, other SEM images from different positions of the samples were used to measure the lamellar spacing and the width of the primary rod-shaped γ -Ni₃₁Si₁₂ grains. At least 30 measurements were carried out to obtain a reliable average value with the help of the software of ImageJ.

see that λ_{fine} (2.5 to 3.9 μm) does not change much with undercooling. This means that the fine lamellar eutectic phase is formed either during recalescence in the case of low undercooling or after recalescence in the case of high undercooling. For both cases, the interface is under a local equilibrium condition. On the other hand, both λ_{coarse} and W_{rod} decrease with undercooling. They are nearly equal when coarse lamellar eutectics and primary rod-shaped γ -Ni₃₁Si₁₂ grains are coexistent. Therefore, the formation of the coarse lamellar eutectic phase might strongly relate to rapid solidification of the primary γ -Ni₃₁Si₁₂ phase (cf. Section IV-A).

C. Growth Velocities and Recalescence Processes

Because rapid solidification releases a large amount of latent heat, the recalescence front can be identified by the brightness difference between the undercooled melt and the solid. Migration of the solid-liquid interface can be described by tracking the loci of the recalescence front. With the help of the software of i-SPEED Suite, the average growth velocity can be determined by dividing the total traveling distance of the recalescence front with the recalescence time. The growth velocity V as a function of undercooling ΔT for rapid solidification in the undercooled Ni-29.8 at. pct Si eutectic alloy is shown in Figure 4. The error bars due to uncertainties in the measurements are set to be ± 20 pct according to Castle *et al.*^[37,38] One can see that the growth velocity first increases slowly, then sharply, and finally almost linearly. Similar growth kinetics was reported in Reference 27. The sharp increase of the growth velocity occurs at about $\Delta T = 100$ K and this is accompanied by the formation of directional rod-shaped γ -Ni₃₁Si₁₂ grains (Figure 2(d)).

Figure 5 shows some typical high-speed video camera images for rapid solidification in the undercooled

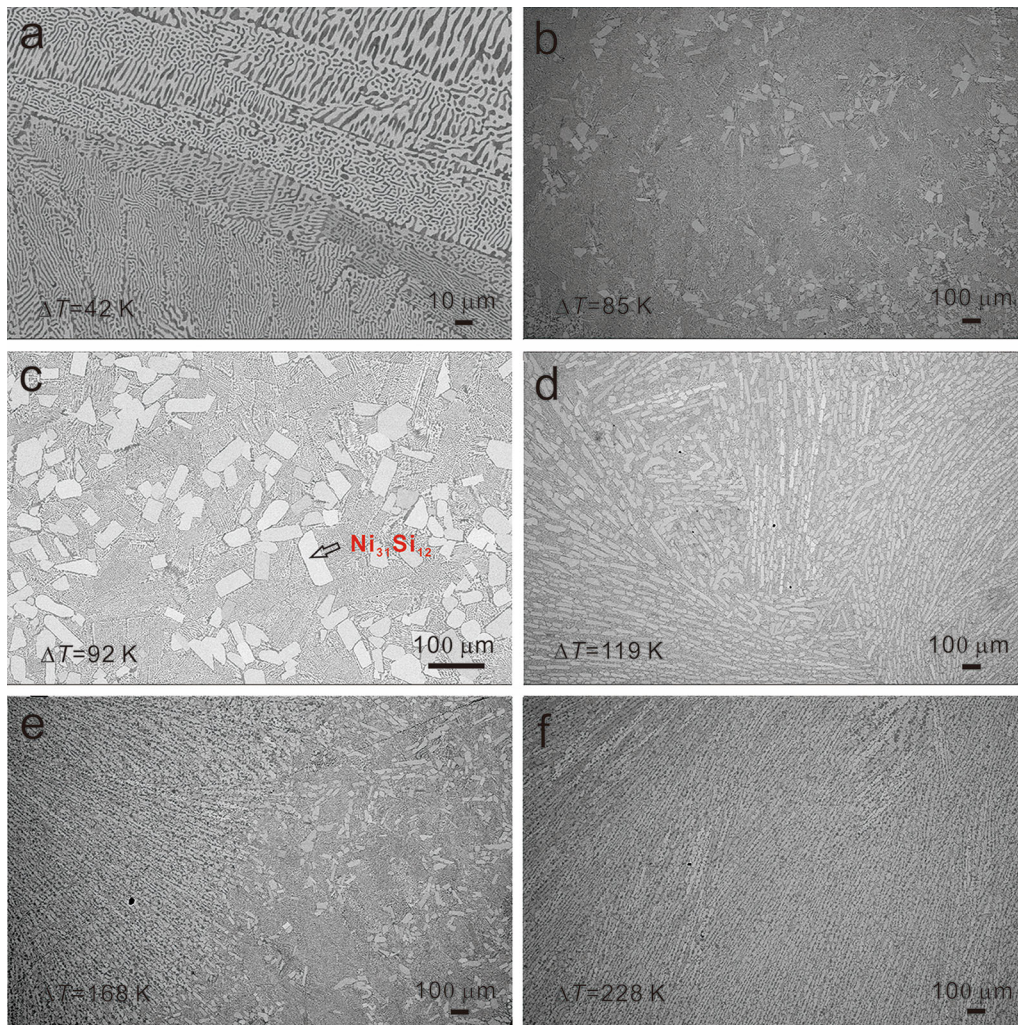


Fig. 2—Microstructures for rapid solidification in the undercooled Ni-29.8 at. pct Si eutectic alloy: (a) $\Delta T = 42$ K; (b) $\Delta T = 85$ K; (c) $\Delta T = 92$ K; (d) $\Delta T = 119$ K; (e) $\Delta T = 168$ K; (f) $\Delta T = 228$ K.

Ni-29.8 at. pct Si eutectic alloy. For $\Delta T = 85$ K, nucleation happens on the surface of the melt where there is a small impurity in white. After that, the recalescence front with many tips grows radially into the melt. In this case, the recalescence front is not sharp but diffuse, *i.e.*, it is a mixture of the primary γ -Ni₃₁Si₁₂ phase and the undercooled melt. For $\Delta T = 92$ K, at which a sharp increase of the growth velocity starts, the growth of the tips in the diffuse recalescence front can be caught up by solidification of the remained melt within the primary γ -Ni₃₁Si₁₂ phase. In this case, the tips become much shorter. For $\Delta T = 119$ K, the recalescence front is still diffuse but the tips are no longer visible. Furthermore, both the volume and width of the remained melt within the primary γ -Ni₃₁Si₁₂ phase become much smaller. In this case, rapid solidification of the primary phase is followed immediately by rapid solidification of the remained melt into the second phase. For $\Delta T = 168$ K, the recalescence front becomes a sharp one. In this case, the solidification of the primary phase and the remained melt in between become indistinguishable.

Accompanied by the sharp increase of the growth velocity, a diffuse one with tips, a diffuse one without tips, and a sharp one occur in sequence for the recalescence front. For the first one, the primary γ -Ni₃₁Si₁₂ phase has more time to be fragmented and rotated, thus resulting in the observed random distribution of rod-shaped grains (cf. Figures 2(b) and (c)). For the second one, fragmentation of the primary γ -Ni₃₁Si₁₂ phase is hindered by rapid solidification of the remained melt within the diffuse recalescence front, thus retaining the initial directional microstructures (cf. Figures 2(d) through (f)).

D. Grain Orientations

The change in the microstructure from a mixture of directional rod-shaped γ -Ni₃₁Si₁₂ grains and fine lamellar eutectics to coarse lamellar eutectics was examined by EBSD. For $\Delta T = 98$ K, the primary γ -Ni₃₁Si₁₂ grains are directional and rod-shaped, around which are the fine lamellar eutectics (cf. Figure 6(a)). Even though the directional γ -Ni₃₁Si₁₂ grains appear to be

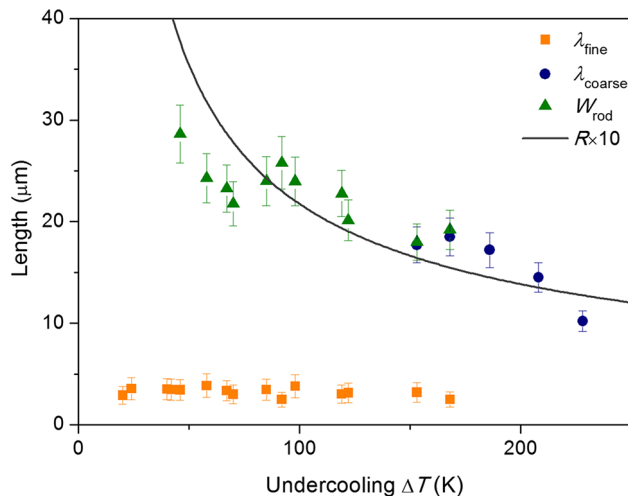


Fig. 3—Measured fine lamellar spacing λ_{fine} , the width of the primary $\gamma\text{-Ni}_{31}\text{Si}_{12}$ intermetallic compound W_{rod} , and coarse lamellar spacing λ_{coarse} in the microstructures for rapid solidification in the undercooled Ni-29.8 at. pct Si eutectic alloy. The error bar is the standard deviation of more than 30 measurements. The predictions of the dendritic trunk, which is assumed to be ten times of the dendritic tip radius (R) of the $\gamma\text{-Ni}_{31}\text{Si}_{12}$ phase, are shown as the solid line.

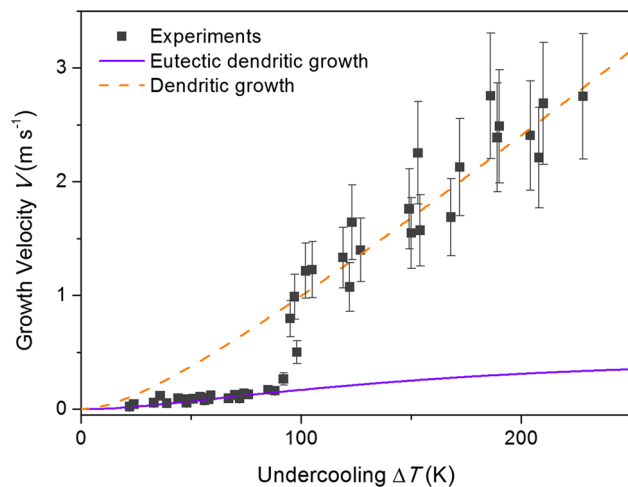


Fig. 4—Growth velocity V as a function of undercooling ΔT for rapid solidification in the undercooled Ni-29.8 at. pct Si eutectic alloy: the solid squares, the experimental measurements; the solid line, the predictions by the eutectic-dendritic growth model; the dashed line, the predictions by the dendritic growth model.

fragmented, the initial microstructure is retained to a large extent. EBSD analysis shows that neighboring rod-shaped grains have similar orientations, being consistent with the one concentrated orientation in the $\langle 0001 \rangle$ pole figure (cf. Figure 6(b)). In addition, there is a small amount of random orientations for the fragments, which can be ascribed to rotation of fragments due to fluid flow.^[39] Particularly, it is always the case that the primary $\gamma\text{-Ni}_{31}\text{Si}_{12}$ phase and the $\gamma\text{-Ni}_{31}\text{Si}_{12}$ phase in the fine lamellar eutectics have the same orientation. So are the neighboring $\delta\text{-Ni}_2\text{Si}$ fine lamellae (cf. Figures 6(b) and (c)). Therefore, epitaxial growth on

the primary rod-shaped $\gamma\text{-Ni}_{31}\text{Si}_{12}$ phase forms the fine lamellar eutectics and the eutectic growth follows a fixed eutectic orientation.

For $\Delta T = 168$ K, the region with only coarse lamellar eutectics, the transition region with coarse lamellar eutectics to a mixture of directional rod-shaped $\gamma\text{-Ni}_{31}\text{Si}_{12}$ grains and fine lamellar eutectics, and the region with only a mixture of directional rod-shaped $\gamma\text{-Ni}_{31}\text{Si}_{12}$ grains, and fine lamellar eutectics were chosen for EBSD analysis (cf. Figures 7, 8, and 9). In Figure 7, a single main orientation for the $\gamma\text{-Ni}_{31}\text{Si}_{12}$ phase and three main orientations for the $\delta\text{-Ni}_2\text{Si}$ phase can be found. The absence of random orientations in the pole figures indicates that coarse lamellar eutectics are the initial solidification microstructures. It should be pointed out that the large dispersion in the main orientations as shown in the insets of Figures 7(b) and (c) is due to radial growth of coarse lamellar eutectics but not rotation of fragments. Ascribing to rotation of fragments and epitaxial growth of fine lamellar eutectics on them, there are some random orientations for both the $\gamma\text{-Ni}_{31}\text{Si}_{12}$ and $\delta\text{-Ni}_2\text{Si}$ phases in Figure 8. Besides some random grains in the region with only directional rod-shaped $\gamma\text{-Ni}_{31}\text{Si}_{12}$ grains and fine lamellar eutectics, the rod-shaped primary $\gamma\text{-Ni}_{31}\text{Si}_{12}$ grains have always similar orientations. Therefore, the $\gamma\text{-Ni}_{31}\text{Si}_{12}$ phase in the coarse lamellar eutectics as well as the directional rod-shaped $\gamma\text{-Ni}_{31}\text{Si}_{12}$ phase should be formed by the same growth mechanism. Besides more random orientations for both the $\gamma\text{-Ni}_{31}\text{Si}_{12}$ and the $\delta\text{-Ni}_2\text{Si}$ phase, the results shown in Figure 9 are the same as those in Figure 6. Since latent heat released continuously to the undercooled melt with migrating recalescence front, undercooling of the remained melt should increase gradually. In this sense, the coarse lamellar eutectic near the nucleation site is formed at relatively higher undercooling, while the directional rod-shaped $\gamma\text{-Ni}_{31}\text{Si}_{12}$ grains distant from the nucleation site are formed at relatively lower undercooling.

For $\Delta T = 228$ K, only coarse lamellar eutectics are formed. Under low magnification, the microstructure observed by SEM is similar to lamellar eutectics but with a much larger lamellar spacing (cf. Figure 2(f)). Under high magnification, the microstructure observed by EBSD, however, is closer to coarse anomalous eutectics^[19,20] (cf. Figure 10(a)). Furthermore,

[†]The fine anomalous eutectics are formed by fragmentation of fine lamellar eutectics.^[19,20]

only a single main orientation and three main orientations can be found for the $\gamma\text{-Ni}_{31}\text{Si}_{12}$ and $\delta\text{-Ni}_2\text{Si}$ phases as shown in Figure 10.

The EBSD results indicate that the primary rod-shaped $\gamma\text{-Ni}_{31}\text{Si}_{12}$ phase and the lamellar $\gamma\text{-Ni}_{31}\text{Si}_{12}$ phase have similar orientations and thus nucleation is not needed to initiate eutectic growth. Growth of the $\gamma\text{-Ni}_{31}\text{Si}_{12}$ and the $\delta\text{-Ni}_2\text{Si}$ phase in coarse lamellar eutectics obeys a fixed orientation relationship. The $\gamma\text{-Ni}_{31}\text{Si}_{12}$ phase is the primary phase and nucleation is

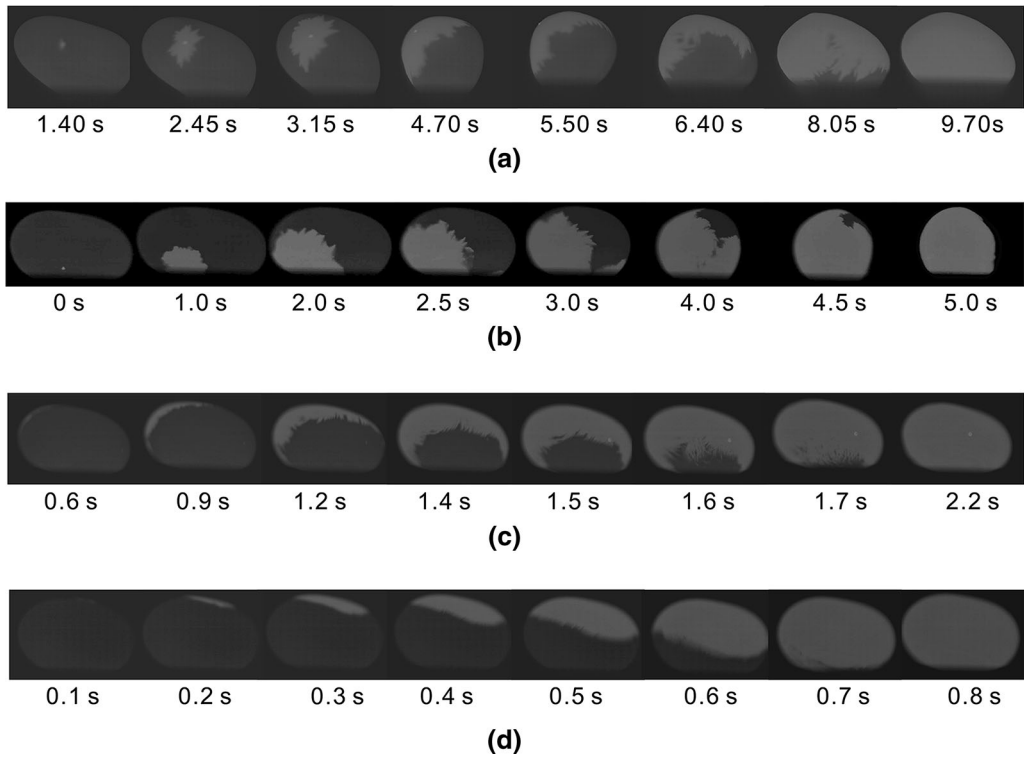


Fig. 5—A typical series of high-speed video camera images for rapid solidification in the undercooled Ni-29.8 at. pct Si eutectic alloy: (a) $\Delta T = 85$ K; (b) $\Delta T = 92$ K; (c) $\Delta T = 119$ K; (d) $\Delta T = 168$ K.

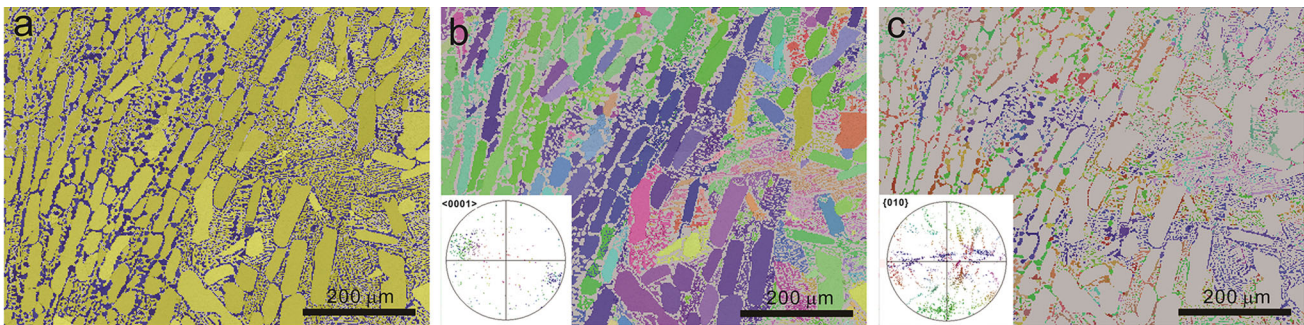


Fig. 6—Map of the phase constituent with the trigonal $\text{Ni}_{31}\text{Si}_{12}$ intermetallic compound in yellow and the orthorhombic Ni_2Si intermetallic compound in blue (a), the EBSD orientation maps for the $\text{Ni}_{31}\text{Si}_{12}$ (b), and the Ni_2Si (c) intermetallic compound at $\Delta T = 98$ K. Insets of (b) and (c) are the $\langle 0001 \rangle$ and the $\{010\}$ pole figure for the $\text{Ni}_{31}\text{Si}_{12}$ and the Ni_2Si intermetallic compound, respectively.

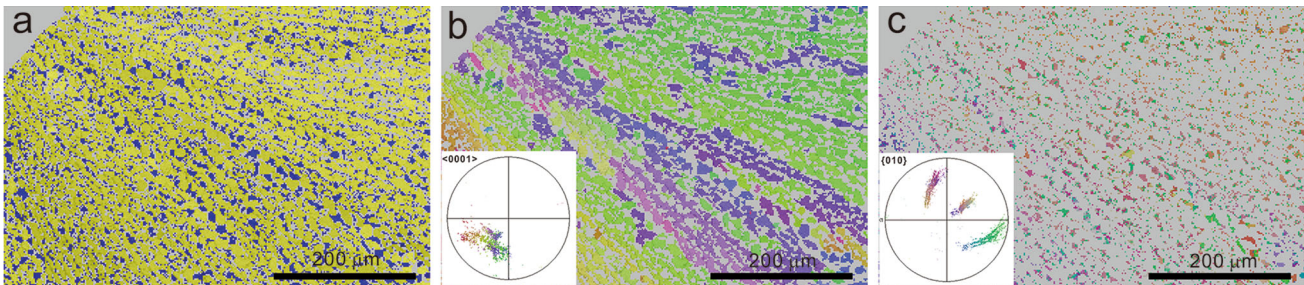


Fig. 7—Map of the phase constituent with the $\text{Ni}_{31}\text{Si}_{12}$ intermetallic compound in yellow and the Ni_2Si intermetallic compound in blue (a), the EBSD orientation maps for the $\text{Ni}_{31}\text{Si}_{12}$ (b), and the Ni_2Si (c) intermetallic compound at $\Delta T = 168$ K. Insets of (b) and (c) are the $\langle 0001 \rangle$ and the $\{010\}$ pole figure for the $\text{Ni}_{31}\text{Si}_{12}$ and the Ni_2Si intermetallic compound, respectively. In this case, the region of coarse lamellar eutectics was chosen.

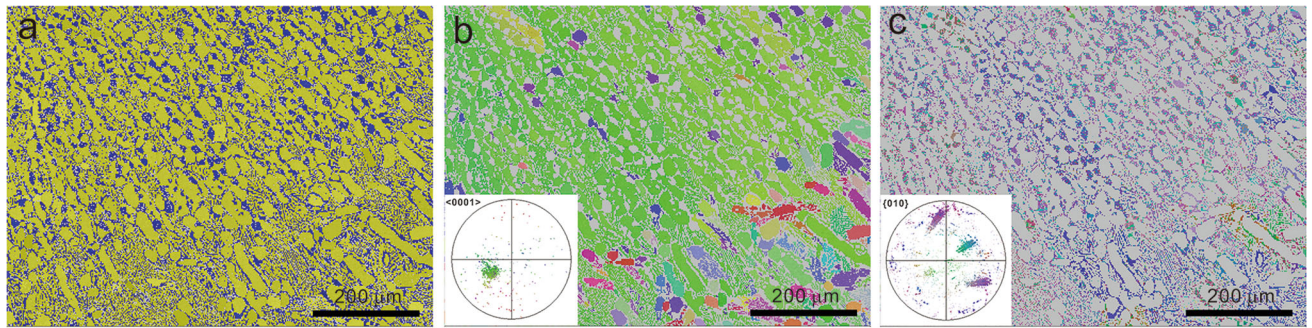


Fig. 8—Map of the phase constituent with the $\text{Ni}_{31}\text{Si}_{12}$ intermetallic compound in yellow and the Ni_2Si intermetallic compound in blue (a), the EBSD orientation maps for the $\text{Ni}_{31}\text{Si}_{12}$ (b), and the Ni_2Si (c) intermetallic compound at $\Delta T = 168$ K. Insets of (b) and (c) are the $\langle 0001 \rangle$ and the $\{010\}$ pole figure for the $\text{Ni}_{31}\text{Si}_{12}$ and the Ni_2Si intermetallic compound, respectively. In this case, the transition region from coarse lamellar eutectics to a mixture of the primary directional rod-shaped $\text{Ni}_{31}\text{Si}_{12}$ intermetallic compound with fine lamellar eutectics was chosen.

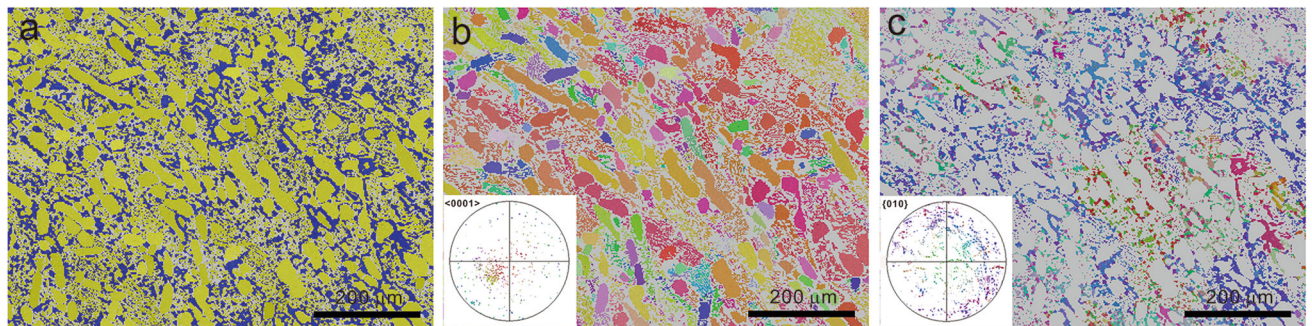


Fig. 9—Map of the phase constituent with the $\text{Ni}_{31}\text{Si}_{12}$ intermetallic compound in yellow and the Ni_2Si intermetallic compound in blue (a), the EBSD orientation maps for the $\text{Ni}_{31}\text{Si}_{12}$ (b), and the Ni_2Si (c) intermetallic compound at $\Delta T = 168$ K. Insets of (b) and (c) are the $\langle 0001 \rangle$ and the $\{010\}$ pole figure for the $\text{Ni}_{31}\text{Si}_{12}$ and the Ni_2Si intermetallic compound, respectively. In this case, the region of the primary directional rod-shaped $\text{Ni}_{31}\text{Si}_{12}$ intermetallic compound and fine lamellar eutectics was chosen.

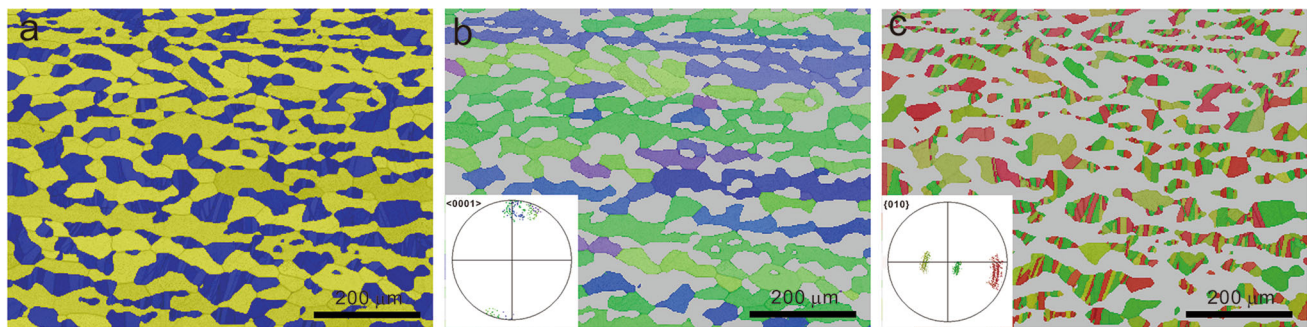


Fig. 10—Map of the phase constituent with the $\text{Ni}_{31}\text{Si}_{12}$ intermetallic compound in yellow and the Ni_2Si intermetallic compound in blue (a), the EBSD orientation maps for the $\text{Ni}_{31}\text{Si}_{12}$ (b), and the Ni_2Si (c) intermetallic compound at $\Delta T = 228$ K. Insets of (b) and (c) are the $\langle 0001 \rangle$ and the $\{010\}$ pole figure for the $\text{Ni}_{31}\text{Si}_{12}$ and the Ni_2Si intermetallic compound, respectively.

not needed to initiate solidification of the second $\delta\text{-Ni}_2\text{Si}$ phase. The absence of nucleation is the reason why solidification of the remained melt into either fine lamellar eutectics or the $\delta\text{-Ni}_2\text{Si}$ phase could catch up with rapid solidification of the primary $\gamma\text{-Ni}_{31}\text{Si}_{12}$ phase as shown in Figure 5.

It should be noted that because the $\gamma\text{-Ni}_{31}\text{Si}_{12}$ phase is solidified as the primary microstructure, subsequent solidification of the secondary $\delta\text{-Ni}_2\text{Si}$ phase within the skeleton of primary phase could result in stress in the solids.^[40,41] In this sense, there is a driving force for

recrystallization, thus leading to many annealing twins in the $\delta\text{-Ni}_2\text{Si}$ grains (cf., e.g., Figure 10(c)). In order to show more information on the triple orientations in the $\delta\text{-Ni}_2\text{Si}$ phase, a refined EBSD analysis with a step size of $0.1 \mu\text{m}$ was carried out (cf. Figure 11). One can see that the $\delta\text{-Ni}_2\text{Si}$ grain are constituted by many small grains. For the $\gamma\text{-Ni}_{31}\text{Si}_{12}$ grain marked by “0” and the small $\delta\text{-Ni}_2\text{Si}$ grains marked by “1,” “2,” and “3” with three different orientation colors, the spatial distribution of their orientations is shown. Accordingly, the triple orientations are formed by rotation about 55 and 65 deg

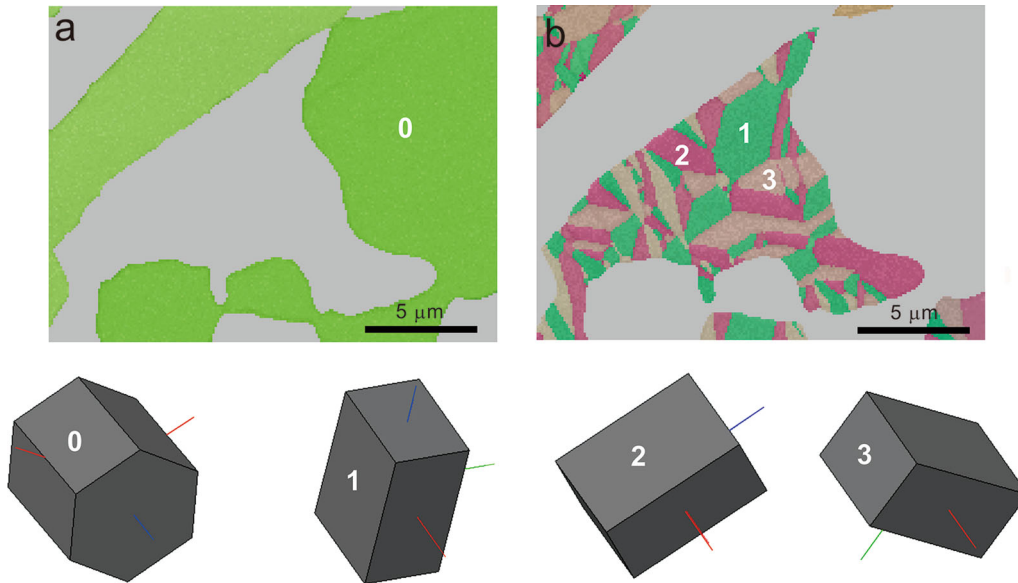


Fig. 11—Triple orientations in the δ -Ni₂Si phase. The EBSD orientation maps for the Ni₃₁Si₁₂ (a) and the Ni₂Si (b) intermetallic compound at $\Delta T = 168$ K as well as the space distribution of the orientations of the γ -Ni₃₁Si₁₂ grain marked by “0” and the small δ -Ni₂Si grains marked by “1,” “2,” and “3” are shown.

with a fixed axis in red. Because the atomic structures of the δ -Ni₂Si and γ -Ni₃₁Si₁₂ phases are rather complex, the Ni and Si atoms are not shown and a definite description of the orientation relationships is not done here. It should be noted that there might be a different reason for this special grain structure in δ -Ni₂Si. For example, it could also be produced by a solid-state phase transition from the high-temperature θ -Ni₂Si phase. This question could be solved by *in-situ* X-ray diffraction investigations during solidification. At present, we believe that a stress-induced twinning mechanism is more probable and the δ -Ni₂Si phase is the primary phase.

IV. DISCUSSION

A. Competition Between Eutectic Growth and Dendritic Growth

In the undercooled Ni-29.8 at. pct Si eutectic alloy, the transition from fine to coarse lamellar eutectics is accompanied by the transition from eutectic growth to single-phase dendritic growth. In this section, the eutectic-dendritic growth model and dendritic growth model are adopted to describe the formation mechanism of coarse lamellar eutectics.

1. Eutectic-dendritic growth model

Based on the thermodynamic extremum principle,^[42,43] work was done to model of eutectic growth, in which the transition at the interface, and solute diffusion in the liquid are under local non-equilibrium conditions.^[28-31] Two new mechanisms for the upper limit of the eutectic growth velocity were found, *i.e.*,

kinetics of the tri-junction and the transition from eutectic growth to single-phase dendritic growth.^[29] In addition, the model predicted reasonably eutectic solidification of the undercooled Ag-Cu eutectic alloy, *e.g.*, when kinetics of tri-junction was considered, the volume fraction of anomalous eutectics can be an order of magnitude larger than the estimated recalescence solid fraction.^[23]

For eutectic growth during which the stoichiometric intermetallic compounds δ -Ni₂Si and γ -Ni₃₁Si₁₂ are solidified from the liquid L, the average kinetic interface condition for migration of the δ /L and γ /L interfaces is^[29]

$$V = \sum_{i=\delta,\gamma} f_i \left[\frac{1}{V_0^{i/L}} + \frac{(\bar{C}_{Li}^* - C_i)^2}{V_{DI}^{i/L} \bar{C}_{Li}^* (1 - \bar{C}_{Li}^*)} \right]^{-1} \times \left\{ 1 - \exp \left[- \frac{C_i \mu_L^{B*} (\bar{C}_{Li}^*) + (1 - C_i) \mu_L^{A*} (\bar{C}_{Li}^*) - g_i + V_m \bar{K}_{i/L} \sigma_{i/L}}{R_g T_i} \right] \right\} \quad [1]$$

Here f_i is the volume fraction of the phase i ($i = \delta, \gamma$) in the solid. $V_0^{i/L}$ is the upper limit of V . $V_{DI}^{i/L}$ is the solute diffusion velocity of the interface. \bar{C}_{Li}^* is the average liquid composition at the i /L interface:

$$\bar{C}_{L\delta}^* = C_\infty + B_0 + \sum_{n=1}^{\infty} \frac{B_n}{n\pi f_\delta} \sin(n\pi f_\delta), \quad [2]$$

$$\bar{C}_{L\gamma}^* = C_\infty + B_0 - \sum_{n=1}^{\infty} \frac{B_n}{n\pi f_\gamma} \sin(n\pi f_\gamma). \quad [3]$$

C_∞ is the initial composition:

$$C_\infty = f_\delta C_\delta + f_\gamma C_\gamma. \quad [4]$$

$$B_0 = C_L^\wedge - C_\infty - \sum_{n=1}^{\infty} B_n \cos(n\pi f_\delta). \quad [5]$$

$$B_n = \frac{2 \sin(n\pi f_\delta)}{\omega_n n \pi} (C_\gamma - C_\delta) \left/ \left[1 - \sum_{m=1}^{\infty} \frac{2 \sin^2(m\pi f_\delta)}{\omega_m m^2 \pi^2 f_\delta f_\gamma} \right] \right. . \quad [6]$$

C_i is the composition of the phase i and is invariable for a stoichiometric intermetallic compound. $\omega_n = [1 + \sqrt{1 + (2n\pi/P_e)^2}]/2$ with $P_e = V\lambda/2D_L$ the Peclet number and D_L the solute diffusion coefficient in the liquid. μ_L^{B*} and μ_L^{A*} are the interfacial chemical potentials of solute B (Si) and solvent A (Ni), respectively. g_i is the molar Gibbs free energy of the phase i . R_g is the gas constant. $\sigma_{i/L}$ is the interface energy. T_I is the interface temperature. C_L^\wedge is the kinetic eutectic composition, which can be determined by the kinetic interface conditions:

$$V = \left[\frac{1}{V_0^{i/L} + \frac{(C_L^\wedge - C_i)^2}{V_{DI}^{i/L} C_L^\wedge (1 - C_L^\wedge)}} \right]^{-1} \times \left\{ 1 - \exp \left[- \frac{C_i \mu_L^{B*} + (1 - C_i) \mu_L^{A*} - g_i + V_m K_{i/L}^\wedge \sigma_{i/L}}{RT_I} \right] \right\}, \quad (i = \delta, \gamma) \quad [7]$$

V_m is the molar volume. The average curvature $\bar{K}_{i/L}$ ^[5] is

$$\bar{K}_{i/L} = \frac{2 \sin \theta_i}{\lambda f_i}, \quad (i = \delta, \gamma). \quad [8]$$

The contact angle θ_i can be obtained by kinetics of the tri-junction:

$$V = M_{TJ} (\sigma_{\delta/L} \sin \theta_\delta + \sigma_{\gamma/L} \sin \theta_\gamma - \sigma_{\delta/\gamma}) \quad \text{and} \quad [9] \\ \sigma_{\delta/L} \cos \theta_\delta - \sigma_{\gamma/L} \cos \theta_\gamma = 0.$$

M_{TJ} is the mobility of the tri-junction. The relation between λ and interface undercooling ($\Delta T_I = T_E^{\text{eq}} - T$) can be determined uniquely for a given V by combining the average interface kinetic condition Eq. [1] with the minimum undercooling principle^[5]:

$$\frac{\partial \Delta T_I}{\partial \lambda} = 0. \quad [10]$$

For the undercooled melts, a negative temperature gradient is imposed to the interface to generate its instability to a eutectic dendrite. For such purely thermal-controlled dendritic growth,^[10,16] the thermal undercooling ΔT_T can be obtained from the Ivantsov solution^[44,45] as

$$\Delta T_T = \frac{\Delta \bar{H}_f}{C_P^L} I_V(P_T), \quad [11]$$

where $\Delta \bar{H}_f (= f_\delta \Delta \bar{H}_f^{\delta} + f_\gamma \Delta \bar{H}_f^{\gamma})$ is the average latent heat of fusion, $(\bar{C}_P^L = f_\delta \bar{C}_P^{L\delta} + f_\gamma \bar{C}_P^{L\gamma})$ is the average specific heat of undercooled melts, $P_T = VR/2\alpha_L$ is the thermal Peclet number, α_L is the thermal diffusion coefficient, and R is the dendrite tip radius. Eq. [11] provides actually the relation between VR and ΔT_T . To obtain a unique solution, a second equation from the solvability theory^[46,47] is needed:

$$R = \left(\frac{\bar{\Gamma}}{\sigma_0 \varepsilon^{7/4}} \right) / [P_T \Delta \bar{H}_f \zeta_T / 2 \bar{C}_P^L], \quad [12]$$

where $\zeta_T = 1/(1 + a_T \varepsilon P_T^2)$, $\bar{\Gamma} = f_\delta \bar{\Gamma}_{L\delta} + f_\gamma \bar{\Gamma}_{L\gamma}$ is the average Gibbs–Thompson coefficient, $\bar{\Gamma}_{Li} = \sigma_{i/L} V_m / \Delta \bar{S}_f^{Li}$ with $\Delta \bar{S}_f^{Li}$ the average entropy of fusion for the i/L interface, ε is the anisotropy coefficient, $\sigma_0 = 1/0.42$, and $a_T = 0.3$. For a given V , R and ΔT_T can be determined by Eqs. [11] and [12].

Noting that the total undercooling $\Delta T = \Delta T_I + \Delta T_T$, a combination of the eutectic growth model with the thermal dendritic growth model results in the eutectic-dendritic growth model, according to which λ , R , and ΔT can be determined for a given V .

2. Dendritic growth model

The dendritic growth model for stoichiometric intermetallic compounds^[29,30] was adopted to describe primary solidification of the γ -Ni₃₁Si₁₂ intermetallic compound. For dendritic growth with a tip radius R , the interface kinetic condition is^[29]

$$V = \left[\frac{1}{V_0} + \frac{(C_L^* - C_S)^2}{V_{DI} C_L^* (1 - C_L^*)} \right]^{-1} \times \left\{ 1 - \exp \left[- \frac{C_S \mu_L^{B*} + (1 - C_S) \mu_L^{A*} - g^i - 2V_m \sigma_{SL}/R}{R_g T_I} \right] \right\}, \quad [13]$$

where C_S is the composition in the solid, σ_{SL} is the interface energy, V_0 is the upper limit of V , and V_{DI} is the solute diffusion velocity of the interface. Selection of the operating state of the dendrite can be described by the solvability theory^[46,47] as

$$R = \left(\frac{\Gamma}{\sigma_0 \varepsilon^{7/4}} \right) / [P_T \Delta H_f \zeta_T / 2 C_P^L], \quad [14]$$

where ΔH_f is the latent heat of fusion, C_P^L is the specific heat of the undercooled melt, and $\Gamma = \sigma_{SL} V_m / \Delta S$ with ΔS the entropy of fusion is the Gibbs–Thompson coefficient. Noting that the undercooling ΔT is a sum of the interface undercooling $\Delta T_I = (T_m - T_I)$ and the thermal undercooling ΔT_T , R and ΔT can be determined uniquely by Eqs. [13] and [14] for a given V .

3. Model predictions

For eutectic-dendritic growth in the undercooled Ni-29.8 at. pct Si eutectic alloy, the thermodynamic assessment of the Ni-Si system^[35,36] is adopted to obtain

the thermodynamic properties of γ -Ni₃₁Si₁₂, δ -Ni₂Si, and L (e.g., g_γ , g_δ , μ_L^{A*} , μ_L^{B*} , $\mu_L^{A\wedge}$, $\mu_L^{B\wedge}$, $\Delta H_f^{L\delta}$, $\Delta \bar{H}_f^{L\gamma}$, $\bar{C}_{pL\delta}$, $\bar{C}_p^{L\gamma}$, $\Delta S_f^{L\delta}$ and $\Delta S_f^{L\gamma}$). According to Aziz and Boettinger,^[48] eutectic growth of the γ -Ni₃₁Si₁₂ and δ -Ni₂Si phases is short-range diffusion-limited and $V_0^{i/L} = fD_L/a$ ($i = \gamma, \delta$) with f the geometrical factor of order unity and a the interatomic spacing (e.g., 1.5 Å) should hold. The temperature-dependent diffusion coefficient $D_L = 2.3 \times 10^{-7} \exp(-64700/RT)$ (m² s⁻¹)^[16] and the solute diffusion velocity of the interface $V_D^{i/L} = V_0^{i/L}/2$ are hence adopted. Other physical parameters used are present in Table I. As shown by the solid line in Figure 4, the eutectic-dendritic growth model predicts well the slow growth stage at low undercooling. Because of epitaxial eutectic growth on the primary γ -Ni₃₁Si₁₂ phase, eutectic solidification is able to catch up with single-phase dendritic growth and eutectic growth dominates the solidification process.

For dendritic growth of the primary γ -Ni₃₁Si₁₂ intermetallic compound in the undercooled Ni-29.8 at. pct Si eutectic alloy, the thermodynamic assessment of the Ni-Si system^[35,36] is adopted to obtain the thermodynamic properties of γ -Ni₃₁Si₁₂ and L (e.g., g_γ , μ_L^{A*} , μ_L^{B*} , ΔH_f , C_p^L , and ΔS_f^L). V_m , α_L , and ε are set to be the same as in the eutectic-dendritic growth model. V_0 is set to be 16 (m s⁻¹) and V_{DI} is set to be half of V_0 (c.f. Table I). As shown by the dashed line in Figure 4, the dendritic growth model predicts well the linear growth stage at high undercooling. Regarding that a linear relation can be assumed between the dendritic trunk (R_{trunk}) and the dendritic tip radius,^[13,14] $R_{trunk} = 10R$ is adopted for the γ -Ni₃₁Si₁₂ intermetallic compound; see the solid line in Figure 3. One can see that the width of the primary γ -Ni₃₁Si₁₂ intermetallic compound W_{rod} and the coarse lamellar spacing λ_{coarse} ^{¶¶} can be also predicted well by

¶¶ It should be pointed out that the widths of the primary γ -Ni₃₁Si₁₂ grains and the secondary δ -Ni₂Si do not deviate from each other significantly; see e.g., Figure 7.

the dendritic growth model.

Combining Figures 3 and 4, at high undercooling, the growth of the coarse lamellar eutectics is in line with the dendrite growth model but not the eutectic-dendritic growth model. In other words, our model predictions indicate that coarse lamellar eutectics at high undercooling is formed by single-phase growth of the primary γ -Ni₃₁Si₁₂ phase and epitaxial growth of the second δ -Ni₂Si phase, i.e., decoupled growth.

B. Origins of Coarse Anomalous Eutectics

In the undercooled Ni-18.7 at. pct Sn eutectic alloy, a transition from coupled eutectic growth to decoupled dendritic growth was found.^[19] At high undercooling, fine and coarse anomalous eutectics coexist. The former is a result of fragmentation of fine lamellar eutectics, while the latter is formed by fragmentation of a primary

phase (α -Ni) and solidification of the inter-dendritic liquid into the second phase (Ni₃Sn). Such dual mechanisms for the formation of anomalous eutectics were proved further by growth kinetics in the undercooled Ni-18.7 at. pct Sn eutectic alloys and EBSD analysis of the as-solidified microstructures.^[20] Anomalous eutectics appear at a critical undercooling and their volume fraction increases with undercooling, i.e., there is a transition from partial to fully anomalous eutectics. For the undercooled Ni-29.8 at. pct Si alloy using the melt fluxing technique,^[27] a common transition from decoupled growth to anomalous eutectics and a unique transition from coarse lamellar eutectics to anomalous eutectics were found at intermediate and high undercooling, respectively; for both cases, the anomalous eutectics belong to coarse anomalous eutectics.

In current work using EML, however, coarse anomalous eutectics were found at low undercooling where fine lamellar eutectics are prevailing and at high undercooling where coarse lamellar eutectics are formed. Their origins are not the same. Figure 12 shows the map of the phase constituent, the EBSD orientation maps of the Ni₃₁Si₁₂, and the Ni₂Si intermetallic compound for $\Delta T = 42$ K. In this case, the remained melt is confined into a very small volume and rotation of fragments by fluid flow is restrained. As a result, random orientations of grains are rare for anomalous eutectics; see Figures 12(b) and (c). At the transition region from anomalous eutectics to fine lamellar eutectics, epitaxial growth of anomalous eutectics on fine lamellar eutectics can be found frequently; see the grains marked by arrows in Figures 12(a) and (c). This indicates that coarse anomalous eutectics at low undercooling are formed by fragmentation of fine lamellar eutectics and subsequent coarsening*.

*Similar results can be found in the undercooled Ag-Cu eutectic alloys,^[23] i.e., coarse anomalous eutectics distribute around the primary lamellar eutectics.

Figure 13 shows the map of the phase constituent, the EBSD orientation maps of the Ni₃₁Si₁₂, and the Ni₂Si intermetallic compound for $\Delta T = 168$ K. In this case, the transition region from coarse lamellar eutectics to a mixture of primary directional rod-shaped γ -Ni₃₁Si₁₂ and fine lamellar eutectics was chosen but the position is much close to the region with only coarse lamellar eutectics. One can see that there are some fine lamellar eutectics within coarse lamellar eutectics. Similar to Figure 8, there are some random orientations for both the γ -Ni₃₁Si₁₂ and the δ -Ni₂Si phases. In contrast to the case at low undercooling, epitaxial growth of fine lamellar eutectics on the primary coarse anomalous eutectics can be frequently found; see the grains marked by arrows in Figure 13. In other words, coarse anomalous eutectics at high undercooling are formed by decoupled eutectics growth, i.e., fragmentation of the primary phase and subsequent solidification of the remained melt into the second phase. Because the

Table I. Physical Parameters Used for the Model Calculations

Parameter		Unit	Value
Interface Energy of the γ/L Interface	$\sigma_{\gamma/L}$	J m^{-2}	0.3 ^[29]
Interface Energy of the δ/L Interface	$\sigma_{\delta/L}$	J m^{-2}	0.5 ^[29]
Interface Energy of the γ/δ Interface	$\sigma_{\gamma/\delta}$	J m^{-2}	0.45 ^[29]
Molar Volume	V_m	$\text{m}^3 \text{mole}^{-1}$	8.2×10^{-6} ^[29]
Mobility of the Tri-junction	M_{TJ}	$\text{m}^3 \text{J}^{-1} \text{s}^{-1}$	0.6 ^[29]
Anisotropy Coefficient	ε	—	0.052
Thermal Diffusivity in the Liquid	α_L	$\text{m}^2 \text{s}^{-1}$	4.8×10^{-5}
Interatomic Spacing	a	\AA	1.5
Diffusion Coefficient	D_L	$\text{m}^2 \text{s}^{-1}$	$2.3 \times 10^{-7} \exp(-64700/RT)$ ^[16]
Upper Limit of V	V_0	m s^{-1}	16
Interfacial Solute Diffusion Velocity	V_{DI}	m s^{-1}	8

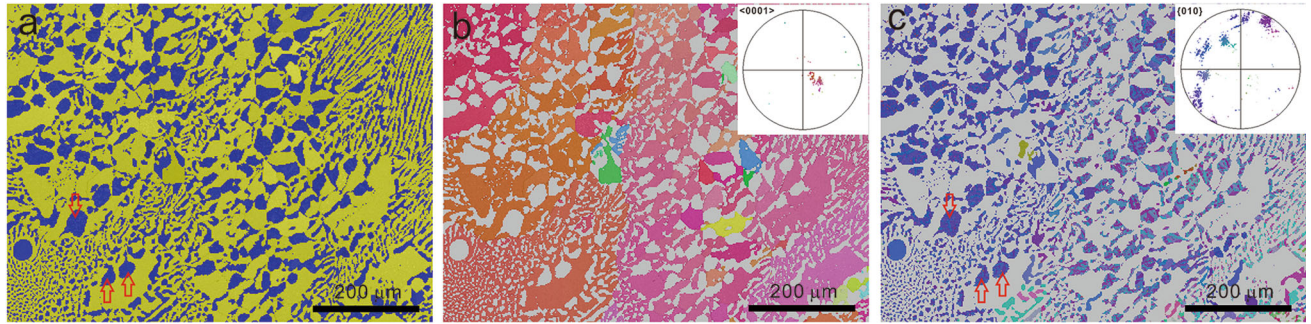


Fig. 12—Map of the phase constituent with the $\text{Ni}_{31}\text{Si}_{12}$ intermetallic compound in yellow and the Ni_2Si intermetallic compound in blue (a), the EBSD orientation maps for the $\text{Ni}_{31}\text{Si}_{12}$ (b), and the Ni_2Si (c) intermetallic compound for $\Delta T = 42$ K. Insets of (b) and (c) are the $\langle 0001 \rangle$ and the $\{010\}$ pole figure for the $\text{Ni}_{31}\text{Si}_{12}$ and the Ni_2Si intermetallic compound, respectively. In this case, the region at the center of the sample was chosen.

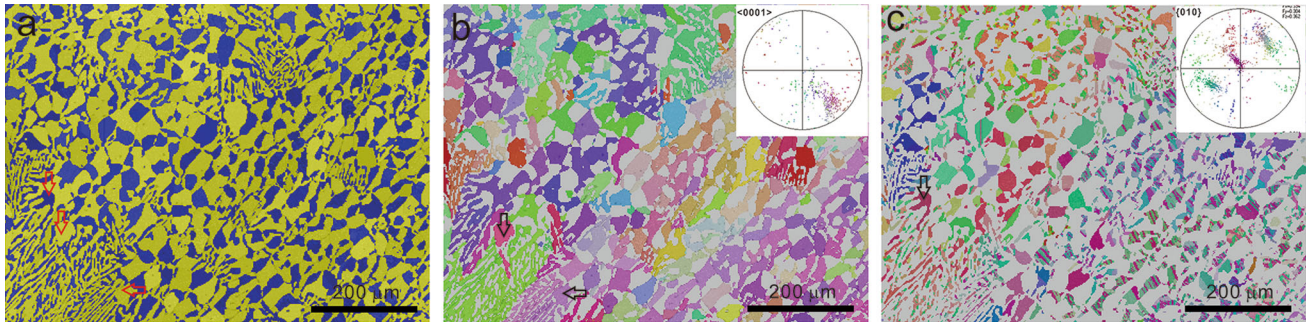


Fig. 13—Map of the phase constituent with the $\text{Ni}_{31}\text{Si}_{12}$ intermetallic compound in yellow and the Ni_2Si intermetallic compound in blue (a), the EBSD orientation maps for the $\text{Ni}_{31}\text{Si}_{12}$ (b), and the Ni_2Si (c) intermetallic compound for $\Delta T = 168$ K. Insets of (b) and (c) are the $\langle 0001 \rangle$ and the $\{010\}$ pole figure for the $\text{Ni}_{31}\text{Si}_{12}$ and the Ni_2Si intermetallic compound, respectively. In this case, the transition region from coarse lamellar eutectics to the mixture of primary directional rod-shaped $\gamma\text{-Ni}_{31}\text{Si}_{12}$ and fine lamellar eutectics was chosen but the analyzing region is much closer to the region with mere coarse lamellar eutectics.

second phase is formed by epitaxial growth, growth of the primary and the second phase is undistinguishable. This indicates that even though the chemical superheating effect is completely absent for the stoichiometric intermetallic compounds, fragmentation of $\gamma\text{-Ni}_{31}\text{Si}_{12}$ could be very quick with the reduction of interface energy as the driving force.

V. CONCLUSIONS

The Ni-29.8 at. pct Si eutectic alloy was undercooled by processing in an electromagnetic levitator. The growth velocity was measured by recording the recalescence process with a high-speed camera. The as-solidified microstructures were analyzed by EBSD. Our main conclusions are as follows:

1. A single recalescence event for rapid solidification in undercooled Ni-29.8 at. pct Si eutectic alloy does not mean that the microstructures are solely eutectics. As undercooling increases, the microstructures transit in sequence from fine lamellar eutectics, to primary random rod-shaped γ -Ni₃₁Si₁₂ grains surrounded by fine lamellar eutectics, to primary directional rod-shaped γ -Ni₃₁Si₁₂ grains surrounded by fine lamellar eutectics, to a mixture of coarse lamellar eutectics and primary directional rod-shaped γ -Ni₃₁Si₁₂ grains surrounded by fine lamellar eutectics, and finally to solely coarse lamellar eutectics.
2. With increasing undercooling, the growth velocity first increases slowly, then sharply, and finally linearly. The sharp increase of the growth velocity occurs at about $\Delta T = 100$ K and this is accompanied by the formation of the directional rod-shaped γ -Ni₃₁Si₁₂ phase. The recalescence front transits from a diffuse one with tips to a diffuse one without tips and then to a sharp one. The slow growth stage at low undercooling and the linear increase growth stage at high undercooling can be predicted well by the eutectic-dendritic growth model and dendritic growth models, respectively.
3. Both the EBSD analysis and the model predictions show that coarse lamellar eutectics are formed by rapid solidification of a primary rod-shaped directional Ni₃₁Si₁₂ intermetallic compound and subsequent epitaxial growth of a secondary Ni₂Si intermetallic compound, *i.e.*, decoupled growth. Nucleation is not needed to initiate eutectic growth or solidification of the remained melt into the second δ -Ni₂Si phase after rapid solidification of the primary rod-shaped γ -Ni₃₁Si₁₂ phase. The triple orientations in the δ -Ni₂Si phase are formed by rotation about 55 and 65 deg.
4. Coarse anomalous eutectics at low undercooling are formed by fragmentation of fine lamellar eutectics and their subsequent coarsening. At high undercooling, they are formed by fragmentation of the primary phase and subsequent solidification of the remained liquid into the second phase. There are two origins for anomalous eutectics, *i.e.*, coupled eutectic growth which can form either coarse or fine anomalous eutectics, and decoupled dendrite growth which leads to coarse anomalous eutectics.

ACKNOWLEDGMENTS

H.F. Wang would like to thank the Huo Yingdong Young Teacher Fund (No. 151048), the Aeronautical Science Foundation of China (No. 2015ZF53066), the Science Fund for Distinguished Young Scholars from Shaanxi province (2018-JC007), and the Fundamental Research Funds for the Central Universities and the support of Alexander von Humboldt Foundation for a research fellowship.

REFERENCES

1. W. Kurz and D.J. Fisher: *Int. Mater. Rev.*, 1979, vol. 24, pp. 177–204.
2. Y.P. Lu, Y. Dong, S. Guo, L. Jiang, H.J. Kang, T.M. Wang, B. Wen, Z.J. Wang, J.C. Jie, Z.Q. Cao, H.H. Ruan, and T.J. Li: *Sci. Rep.*, 2014, vol. 4, p. 6200.
3. Y.P. Lu, X.Z. Gao, L. Jiang, Z.N. Chen, T.M. Wang, J.C. Jie, H.J. Kang, Y.B. Zhang, S. Guo, H.H. Ruan, Y.H. Zhao, Z.Q. Cao, and T.J. Li: *Acta Mater.*, 2017, vol. 124, pp. 143–50.
4. D.M. Herlach: *Mater. Sci. Eng. R*, 1994, vol. 12, pp. 177–272.
5. K.A. Jackson and J.D. Hunt: *Trans. AIME*, 1966, vol. 236, pp. 1129–42.
6. R. Trivedi, P. Magnin, and W. Kurz: *Acta Metall.*, 1987, vol. 35, pp. 971–80.
7. N. Wang, Y.E. Kalay, and R. Trivedi: *Acta Mater.*, 2011, vol. 59, pp. 6604–19.
8. R. Trivedi and N. Wang: *Acta Mater.*, 2012, vol. 60, pp. 3140–52.
9. H.L. Huang, C.L. Yang, Q.J. Song, K. Ye, and F. Liu: *J. Appl. Phys.*, 2016, vol. 120, p. 043905.
10. J.F. Li and Y.H. Zhou: *Acta Mater.*, 2005, vol. 53, pp. 2351–59.
11. L. Liu, J.F. Li, and Y.H. Zhou: *Acta Mater.*, 2009, vol. 57, pp. 1536–45.
12. X.X. Wei, X. Lin, W. Xu, Q.S. Huang, M. Ferry, J.F. Li, and Y.H. Zhou: *Acta Mater.*, 2015, vol. 95, pp. 44–56.
13. M. Schwarz, A. Karma, K. Eckler, and D.M. Herlach: *Phys. Rev. Lett.*, 1994, vol. 73, pp. 1380–83.
14. A. Karma: *Int. J. Non-Equilib. Process.*, 1998, vol. 11, pp. 201–33.
15. H.F. Wang, F. Liu, and Y.M. Tan: *Acta Mater.*, 2011, vol. 59, pp. 4787–97.
16. R. Goetzinger, M. Barth, and D.M. Herlach: *Acta Mater.*, 1998, vol. 46, pp. 1647–55.
17. B.B. Wei, G.C. Yang, and Y.H. Zhou: *Acta Metall. Mater.*, 1991, vol. 39, pp. 1249–58.
18. M.J. Li, K. Nagashio, T. Ishikawa, S. Yoda, and K. Kuribayashi: *Acta Mater.*, 2005, vol. 53, pp. 731–41.
19. J.F. Li, W.Q. Jie, S. Zhao, and Y.H. Zhou: *Metall. Mater. Trans. A*, 2007, vol. 38A, pp. 1806–16.
20. C. Yang, J. Gao, Y.K. Zhang, M. Kolbe, and D.M. Herlach: *Acta Mater.*, 2011, vol. 59, pp. 3915–26.
21. X. Lin, Y.Q. Cao, Z.T. Wang, J. Cao, L.L. Wang, and W.D. Huang: *Acta Mater.*, 2017, vol. 126, pp. 210–20.
22. C.R. Clopet, R.F. Cochrane, and A.M. Mullis: *Acta Mater.*, 2013, vol. 61, pp. 6894–6902.
23. A.M. Mullis and C.R. Clopet: *Acta Mater.*, 2018, vol. 145, pp. 186–95.
24. M.J. Li, K. Nagashio, T. Ishikawa, A. Mizuno, M. Adachi, M. Watanabe, S. Yoda, K. Kuribayashi, and Y. Katayama: *Acta Mater.*, 2007, vol. 56, pp. 2514–25.
25. Y.K. Zhang, J. Gao, M. Kolbe, S. Klein, C. Yang, H. Yasuda, D.M. Herlach, and C.A. Gandin: *Acta Mater.*, 2013, vol. 61, pp. 4861–73.
26. Y.P. Lu, X. Lin, G.C. Yang, J.J. Li, and Y.H. Zhou: *J. Appl. Phys.*, 2008, vol. 104, p. 013535.
27. F. Zhang, C. Lai, J.B. Zhang, Y.C. Zhang, Q. Zhou, and H.F. Wang: *J. Cryst. Growth*, 2018, vol. 495, pp. 37–45.
28. H.F. Wang, F. Liu, and D.M. Herlach: *J. Cryst. Growth*, 2014, vol. 389, pp. 68–73.
29. H.F. Wang, F. Liu, and D.M. Herlach: *J. Mater. Sci.*, 2015, vol. 50, pp. 176–88.
30. W.W. Kuang, H.F. Wang, F. Liu, and S.L. Sobolev: *J. Mater. Sci.*, 2016, vol. 51, pp. 2141–52.
31. W.W. Kuang, C. Karrasch, H.F. Wang, F. Liu, and D.M. Herlach: *Scr. Mater.*, 2015, vol. 105, pp. 34–37.
32. H.F. Wang, F. Liu, and D.M. Herlach: *J. Mater. Sci.*, 2014, vol. 49, pp. 1537–43.
33. H. Wang, D.M. Herlach, and R.P. Liu: *EPL*, 2014, vol. 105, p. 36001.
34. P. Nash and A. Nash: *J. Phase Equilib.*, 1987, vol. 8, pp. 6–14.
35. Y. Du and J.C. Schuster: *Metall. Mater. Trans. A*, 1999, vol. 30A, pp. 2409–17.
36. J.C. Schuster and Y. Du: *Metall. Mater. Trans. A*, 2000, vol. 31A, pp. 1795–1803.

37. E.G. Castle, A.M. Mullis, and R.F. Cochrane: *Acta Mater.*, 2014, vol. 66, pp. 378–87.
38. E.G. Castle, A.M. Mullis, and R.F. Cochrane: *Acta Mater.*, 2014, vol. 77, pp. 76–84.
39. H.F. Wang, F. Liu, and G.C. Yang: *J. Mater. Res.*, 2010, vol. 25, pp. 1963–74.
40. A.K. Dahle, D.H.S. John, H.J. Thevik, and L. Arnberg: *Metall. Mater. Trans. B*, 1999, vol. 30B, pp. 287–93.
41. K. Dragnevski, A.M. Mullis, D.J. Walker, and R.F. Cochrane: *Acta Mater.*, 2002, vol. 50, pp. 3743–55.
42. J. Svoboda, I. Turek, and F.D. Fischer: *Philos. Mag.*, 2005, vol. 85, pp. 3699–3707.
43. F.D. Fischer, J. Svoboda, and H. Petryk: *Acta Mater.*, 2014, vol. 67, pp. 1–20.
44. S. Li, J. Zhang, and P. Wu: *Metall. Mater. Trans. A*, 2012, vol. 43A, pp. 3748–54.
45. S. Li, D.Y. Li, S.C. Liu, Z.H. Gu, W. Liu, and J.W. Huang: *Acta Mater.*, 2015, vol. 83, pp. 310–17.
46. P.K. Galenko, S. Reutzel, D.M. Herlach, D. Danilov, and B. Nestler: *Acta Mater.*, 2007, vol. 55, pp. 6834–42.
47. P.K. Galenko, S. Reutzel, D.M. Herlach, S.G. Fries, I. Steinbach, and M. Apel: *Acta Mater.*, 2009, vol. 57, pp. 6166–75.
48. M.J. Aziz and W.J. Boettinger: *Acta Metall. Mater.*, 1994, vol. 42, pp. 527–37.

Publisher's Note Springer Nature remains neutral with regard to jurisdictional claims in published maps and institutional affiliations.